

## RESEARCH ARTICLE

View Article Online  
View Journal | View Issue

Cite this: *Mater. Chem. Front.*,  
2023, 7, 1395

Steering CO<sub>2</sub> electroreduction selectivity towards  
CH<sub>4</sub> and C<sub>2</sub>H<sub>4</sub> on a tannic acid-modified  
Cu electrode†

Keqiang Xu,<sup>a</sup> Jinhan Li,<sup>a</sup> Fangming Liu,<sup>a</sup> Wence Xu,<sup>a</sup> Tete Zhao<sup>a</sup> and  
Fangyi Cheng <sup>\*ab</sup>

CO<sub>2</sub> electroreduction (CO<sub>2</sub>RR) offers a promising way to address CO<sub>2</sub> emission and high-value utilization but it remains challenging to steer the selectivity of products due to complicated reaction pathways. Herein, tannic acid (TA) is reported as a modifier to regulate the selectivity of C<sub>2</sub>H<sub>4</sub> and CH<sub>4</sub> over the Cu catalyst. With an optimized TA amount, the maximal Faradaic efficiency of C<sub>2</sub>H<sub>4</sub> and CH<sub>4</sub> increases from 35.46% and 18.56% to 53.00% and 53.27%, respectively. *In situ* attenuated total reflection surface-enhanced infrared absorption spectra demonstrate that TA modification stabilizes the adsorbed CO and CHO intermediate and strengthens the interaction of hydrogen bonds with H<sub>2</sub>O. Kinetic isotope effect analysis of H<sub>2</sub>O/D<sub>2</sub>O reveals that TA-modified Cu could activate H<sub>2</sub>O dissociation to accelerate the proton-coupled electron transfer. Theoretical calculations further indicate the decrease of the energy barrier from \*CO hydrogenation to \*CHO by TA modification. The results evidence the importance of molecule modification to tailor the C<sub>2</sub>/C<sub>1</sub> product selectivity in the CO<sub>2</sub>RR via concurrently stabilizing the intermediate and promoting proton transfer.

Received 5th December 2022,  
Accepted 30th January 2023

DOI: 10.1039/d2qm01259f

rsc.li/frontiers-materials

## Introduction

Recently, the electrocatalytic CO<sub>2</sub> reduction reaction (CO<sub>2</sub>RR) powered by renewable energy has attracted much attention, as it not only reduces CO<sub>2</sub> emission but also produces chemicals.<sup>1,2</sup> Among the catalysts reported for the CO<sub>2</sub>RR, copper-based nanomaterials are promising in generating multi-electron (>2e<sup>−</sup>) products due to the positive adsorption energy for \*H and negative adsorption energy for \*CO.<sup>3–8</sup> Compared to the two electron products (e.g., CO and HCOOH) in the CO<sub>2</sub>RR,<sup>9–12</sup> the multi-electron products (e.g., CH<sub>4</sub>, C<sub>2</sub>H<sub>4</sub>, CH<sub>3</sub>CH<sub>2</sub>OH, CH<sub>3</sub>CH<sub>2</sub>CH<sub>2</sub>OH, etc.) are more desired with higher economic value since hydrocarbons such as CH<sub>4</sub> and C<sub>2</sub>H<sub>4</sub> are attractive due to their easy transport, convenient storage and high energy value.<sup>13</sup> However, it is difficult to tailor the selectivity of hydrocarbons because of multiple reaction pathways and the competing hydrogen evolution reaction (HER) in the CO<sub>2</sub>RR. In the process of the CO<sub>2</sub>RR on Cu catalysts, there are two significant factors having crucial effects on the selectivity of hydrocarbons.<sup>14,15</sup> On the one hand, the intermediate (i.e., \*CO) would be stabilized on the Cu surface to

prevent CO release. On the other hand, the formation of hydrocarbon involves multiple proton-coupled electron transfer (PCET) processes, making it essential to accelerate the PCET to improve the sluggish kinetics. However, the high local pH near the surface of the electrode retards the dissociation of water to provide protons.<sup>16,17</sup> Moreover, the \*CHO intermediate is a key species to generate hydrocarbons in the CO<sub>2</sub>RR.<sup>18,19</sup> Therefore, stabilizing \*CO species and activating water are of paramount importance for the hydrogenation of \*CO to \*CHO to form hydrocarbons.

Molecular modification of electrocatalysts exerts a significant effect on the CO<sub>2</sub>RR.<sup>20,21</sup> Molecules such as amino acid,<sup>22</sup> poly(acrylamide),<sup>23</sup> polypyrrole<sup>24</sup> and polyaniline<sup>25</sup> can stabilize intermediates to facilitate the selectivity of hydrocarbons through the interaction of hydrogen bonds with \*CHO or CO dimer intermediates. According to the density functional theory (DFT) results, hydrogen bonds could decrease the energy barrier for \*CO protonation to the \*CHO intermediate.<sup>26</sup> In addition to stabilizing the intermediate, hydrogen bonds could function as a “proton pump” to promote the transfer of protons by stabilizing OH<sup>−</sup> of H<sub>2</sub>O or act as a “bridge” to promote proton transportation in electrochemical reactions.<sup>27–30</sup> Thus, we expect that molecules that can construct hydrogen bonds would stabilize the intermediate and boost proton transfer to enhance the selectivity of hydrocarbon in the CO<sub>2</sub>RR. Among the reported functional groups, −OH or −NH<sub>2</sub> is shown to form hydrogen bonds with intermediates.<sup>25,31</sup> Moreover, molecules should be firmly modified on the surface of electrodes to

<sup>a</sup> Key Laboratory of Advanced Energy Materials Chemistry (Ministry of Education), Renewable Energy Conversion and Storage Center, College of Chemistry, Nankai University, Tianjin 300071, China. E-mail: fycheng@nankai.edu.cn

<sup>b</sup> Engineering Research Center of High-efficiency Energy Storage (Ministry of Education), Tianjin 300071, China

† Electronic supplementary information (ESI) available. See DOI: <https://doi.org/10.1039/d2qm01259f>

maintain stability during electrocatalysis. Taking the above factors into consideration, we select tannic acid (TA, structurally shown in Fig. S1, ESI†) to investigate its effect on hydrocarbon generation in the CO<sub>2</sub>RR. Note that TA, which has been found widely in plants, features abundant phenolic hydroxyl and carbonyl groups<sup>32</sup> and could be coated on nanoparticles steadily *via* covalent or non-covalent interactions.<sup>33</sup> Besides, TA has also been reported to improve the performance of zinc ion batteries and electrocatalysis as a result of hydrogen interaction and adsorption effects.<sup>34,35</sup> It is attractive and worth investigating the functionalization effect of TA as a molecular modifier to modulate the selectivity of the Cu electrode, which has not been reported to the best of our knowledge.

In this work, we modify tannic acid molecules on the surface of Cu and investigate their effects on the selectivity of hydrocarbons in the CO<sub>2</sub>RR. We demonstrate surface TA functionalization to regulate the selectivity over the Cu catalyst and the selectivity of hydrocarbon transformation from C<sub>2</sub>H<sub>4</sub> to CH<sub>4</sub> with an increasing amount of modified TA. *In situ* attenuated total reflection surface-enhanced infrared absorption spectra reveal that TA modification could stabilize \*CO and \*CHO intermediates and enhance hydrogen bond interaction with H<sub>2</sub>O near the electrode surface. Kinetic isotope effect experiments verify facilitated dissociation of H<sub>2</sub>O assisted by TA to promote \*CO hydrogenation. DFT calculations further validate that the TA-functionalized Cu catalyst would stabilize the \*CO intermediate and reduce the energy barrier for the \*CO to \*CHO process. This study suggests the promising use of TA as an efficient modifier to enhance the selectivity of hydrocarbons in the CO<sub>2</sub>RR on Cu catalysts.

## Results and discussion

Fig. 1 schematically shows the process of CO<sub>2</sub>RR on a Cu catalyst with or without TA modification. In the absence of the TA molecule, the primary products of CO<sub>2</sub>RR on Cu are H<sub>2</sub> and C<sub>2</sub>H<sub>4</sub>. In the presence of TA on a Cu surface, the adsorbed CO (denoted as \*CO), which is generated from CO<sub>2</sub> reduction and acts as the intermediate for further reduction, would be stabilized by hydrogen bonds constructed by TA molecules. Besides, H<sub>2</sub>O can be activated to accelerate dissociation to produce protons (\*H) with the assistance of TA molecules. The \*CO could then combine with \*H to produce \*CHO that is an important intermediate for the formation of hydrocarbons. Furthermore, the modification of more TA would activate more H<sub>2</sub>O to produce more \*H, leading to more \*CHO intermediate generation. Accordingly, the product selectivity of C<sub>2</sub>H<sub>4</sub> and CH<sub>4</sub> is expected to be tailorable by adjusting the amount of modified TA.

Fig. S2 (ESI†) illustrates the process of the preparation of Cu and Cu-TA nanoparticles (NPs). Firstly, Cu NPs were synthesized by heating a mixture of Cu(OAc)<sub>2</sub>·H<sub>2</sub>O and sodium ascorbate at 100 °C for 3 h.<sup>36</sup> Then, the obtained Cu NPs were mixed with a desired amount of TA in ethanol solution and ultrasonicated for 0.5 h to prepare Cu-*x*TA (*x* represented the designated mass ratio of TA:Cu). The actual mass fraction of

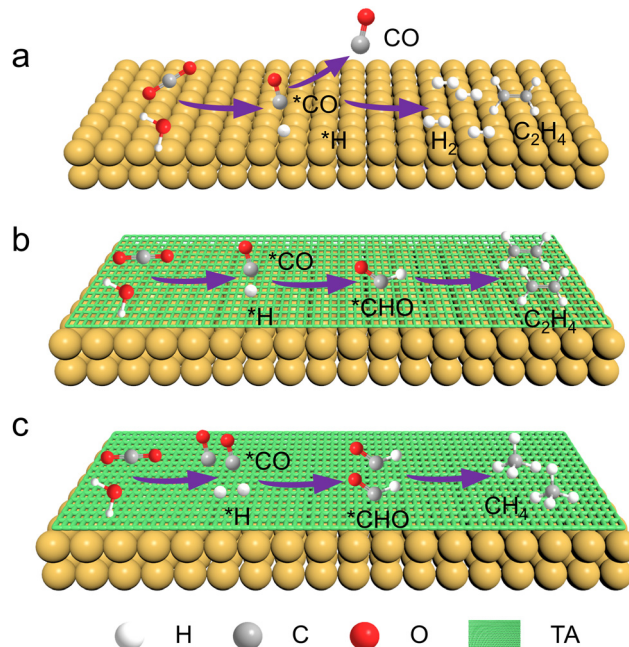


Fig. 1 Schematic illustration of CO<sub>2</sub>RR on the surfaces of (a) Cu, (b) Cu-1TA and (c) Cu-3TA catalysts.

TA in Cu-*x*TA (*x* from 0.5 to 4) samples is 22.45%, 31.38%, 48.99%, 58.48% and 65.89%, which is determined by thermogravimetric analysis (TGA, Fig. S3, ESI†). The prepared samples were characterized by scanning electron microscopy (SEM) and transmission electron microscopy (TEM). As shown in Fig. S4 (ESI†) and Fig. 2a, Cu NPs present a uniform spherical shape. From the high-resolution TEM (HRTEM) image (Fig. 2b), the lattice distance is 0.20 nm, which belongs to the (111) crystal plane of Cu. Additionally, selected area electron diffraction (SAED, Fig. 2c) and X-ray diffraction (XRD, Fig. S5, ESI†) indicates the polycrystalline feature of the prepared Cu NPs with the preferentially exposed (111) crystal plane.

Microscopy and spectroscopies were performed to analyse TA modified Cu NPs. From TEM images (Fig. 2d and Fig. S6, ESI†), Cu-1TA and Cu-3TA show a spherical core-shell structure with a coating layer thickness of 4.5 and 12 nm, respectively. Fig. 2e comparatively displays the Fourier transform infrared (FTIR) spectra of Cu, Cu-1TA and Cu-3TA NPs. Compared with neat Cu NPs, the FTIR curves of Cu-TA NPs exhibit characteristic peaks of TA molecules at a wavenumber of 1700 cm<sup>-1</sup> (C=O stretching vibration), 1483 cm<sup>-1</sup> (aromatic C=C stretching vibration), 1342 and 1195 cm<sup>-1</sup>, (C-O stretching), and 759 cm<sup>-1</sup> (C-H out-plane bending), confirming the modification of TA on Cu. In addition, we carried out the X-ray photoelectron spectroscopy (XPS) measurements. The full spectrum and high-resolution Cu 2p spectra are shown in Fig. S7 (ESI†) and Fig. 2f, respectively. For Cu and Cu-TA NPs, there are two peaks at 932.5 and 952.5 eV, which could be assigned to signals of Cu 2p<sub>3/2</sub> and Cu 2p<sub>1/2</sub>, respectively. Satellite peaks of Cu<sup>2+</sup> are not discernible, indicating good preservation of the metallic state of Cu NPs. The XRD analysis further suggests no

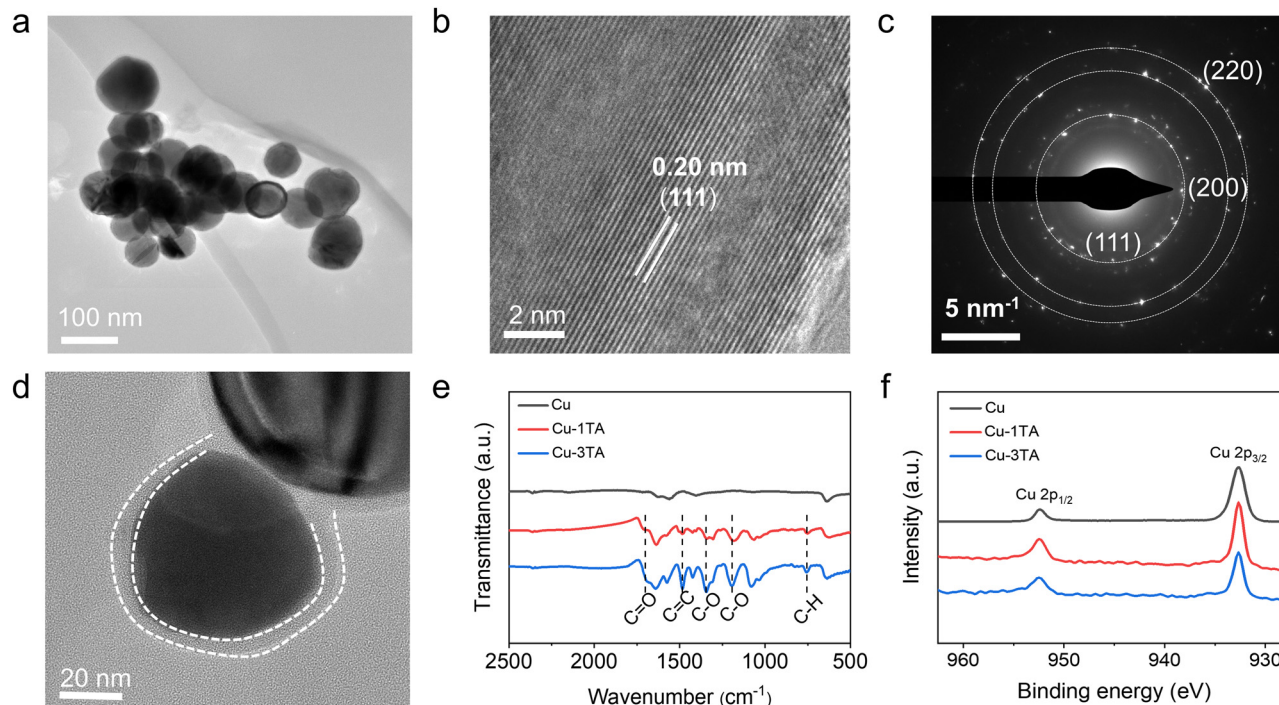


Fig. 2 Typical (a) TEM, (b) HRTEM and (c) SAED images of Cu NPs. (d) TEM image of Cu-1TA NPs. (e) FTIR and (f) XPS spectra of Cu, Cu-1TA and Cu-3TA NPs.

apparent difference of the crystal phase between Cu, Cu-1TA and Cu-3TA NPs (Fig. S5, ESI†).

The CO<sub>2</sub>RR activity of Cu and Cu-TA catalysts was evaluated in a gas-tight H-Cell using a Nafion-117 proton exchange membrane (Fig. S8, ESI†). Linear sweep voltammetry (LSV) curves were conducted in Ar or CO<sub>2</sub>-saturated 0.1 M aqueous KHCO<sub>3</sub> solution. The higher current density in CO<sub>2</sub>-saturated solution than in Ar-saturated solution (Fig. S9, ESI†) indicates the CO<sub>2</sub>RR activity of prepared catalysts. The electrochemical double layer capacitance, which correlates with the electrochemical surface area (ECSA) is 39.73, 38.64 and 33.67 μF for Cu, Cu-1TA and Cu-3TA, respectively (Fig. S10, ESI†). Thus, the surface modification of TA exerts only a slight impact on the exposed active sites of Cu catalysts. Meanwhile, there is a slight increase of charge transfer resistance ( $R_{ct}$ ) after TA modification, as shown in the electrochemical impedance spectroscopy (EIS) spectra (Fig. S11, ESI†). Besides, we measured OH<sup>−</sup> adsorption and desorption behaviour to investigate the influence of TA on Cu NPs. The OH<sup>−</sup> adsorption potential is related to the crystal planes of Cu NPs<sup>37</sup> and the redox potential around 0.54 V in the polarization curves indicates OH<sup>−</sup> adsorption on the Cu(111) facet.<sup>38</sup> As viewed from the discernible positive shift of the anodic peak potential (Fig. S12, ESI†), TA modification retards OH<sup>−</sup> adsorption on the Cu catalyst. Furthermore, the lower OH<sup>−</sup> adsorption current again indicates that the OH<sup>−</sup> adsorption is suppressed on Cu-TA catalysts, which could be explained by the covering of TA on the surface of Cu NPs.

To further evaluate the product distribution for catalysts, on-line gas chromatography (GC) and *ex situ* nuclear magnetic resonance (NMR) spectroscopy were conducted to determine

gas and liquid products (Fig. S13, ESI†), respectively. Fig. S14 (ESI†) shows the faradaic efficiency (FE) of all products and chronoamperometry curves for the Cu catalyst. Main products are H<sub>2</sub> and C<sub>2</sub>H<sub>4</sub> and the FE of H<sub>2</sub> and C<sub>2</sub>H<sub>4</sub> reach up to 48.01% and 35.46% at −1.2 V, respectively. The high selectivity of H<sub>2</sub> decreases the CO<sub>2</sub>RR activity of the Cu catalyst, which is adverse for the CO<sub>2</sub>RR. We then tested different Cu-*x*TA (*x* from 0.5 to 4) catalysts to determine the optimized TA modification amount. Fig. 3a and b show FE distribution curves of C<sub>2</sub>H<sub>4</sub> and CH<sub>4</sub> at −1.2 V and −1.4 V, respectively. Interestingly, the FE of C<sub>2</sub>H<sub>4</sub> decreases and CH<sub>4</sub> increases with an increasing amount of modified TA. For the Cu-1TA catalyst, the FE of C<sub>2</sub>H<sub>4</sub> increases to 53.00% from 35.46% at −1.2 V, which shows the highest C<sub>2</sub>H<sub>4</sub> selectivity among the Cu-TA catalysts. Moreover, our results show a superior performance in comparison with reported results among molecule modified Cu-based catalysts (Table S1, ESI†). For the Cu-3TA catalyst, the FE of CH<sub>4</sub> reaches 36.32% at −1.4 V, which is about 11 times as large as the unmodified Cu catalyst (FE of CH<sub>4</sub> is 3.31% at −1.4 V). The above results indicate the selectivity of C<sub>2</sub>H<sub>4</sub> and CH<sub>4</sub> could be steered *via* adjusting the TA modification amount. Thus, we focus on Cu-1TA and Cu-3TA catalysts to explore the effect of TA modification. The FE of all products and chronoamperometry curves of Cu-1TA and Cu-3TA catalysts at different potentials are shown in Fig. S15 (ESI†) in detail. Fig. 3c and d show FE of C<sub>2</sub>H<sub>4</sub> and CH<sub>4</sub> for Cu, Cu-1TA and Cu-3TA catalysts under different potentials, respectively. The results clearly showcase the transformation of selectivity from C<sub>2</sub>H<sub>4</sub> to CH<sub>4</sub> with increasing amounts of modified TA and the FE of C<sub>2</sub>H<sub>4</sub> decreases and CH<sub>4</sub> increases from the Cu-1TA to the Cu-3TA



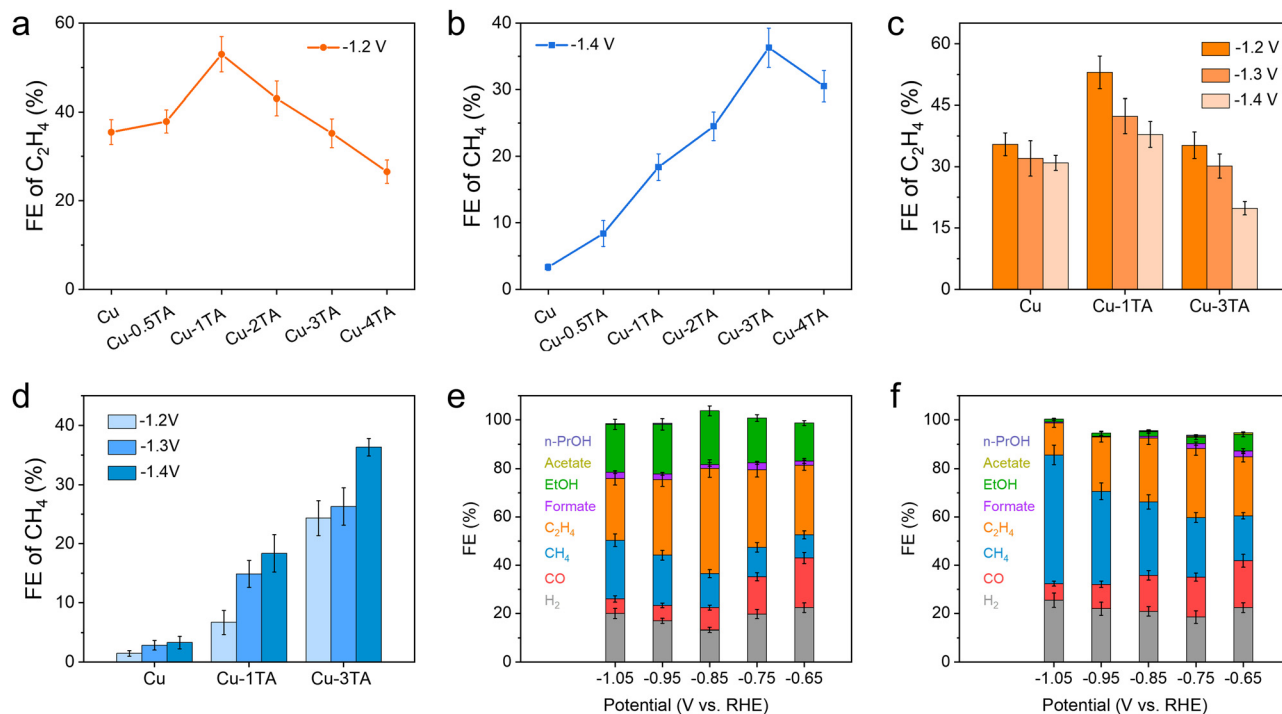


**Fig. 3** (a and b) Faradaic efficiency (FE) of  $C_2H_4$  and  $CH_4$  on Cu and Cu-xTA (x from 0.5 to 4) catalysts in  $CO_2$ -saturated 0.1 M  $KHCO_3$  solution in H-Cell. (c and d) FE of  $C_2H_4$  and  $CH_4$  on Cu, Cu-1TA and Cu-3TA catalysts under different potentials in H-Cells. (e and f) FE of products distribution on Cu-1TA and Cu-3TA catalysts at different applied potential in 1 M  $KHCO_3$  solution in flow cells.

catalyst. We also performed stability tests and FE of  $C_2H_4$  still maintains 50.06% after lasting for 14 000 s for the Cu-1TA catalyst, revealing that Cu-1TA has considerable stability (Fig. S16, ESI†). Moreover, from the SEM and TEM images collected after electrolysis, there is no apparent morphological evolution for the Cu-1TA catalyst (Fig. S17 and S18, ESI†). The FTIR spectrum further evidences the presence of TA on the Cu surface (Fig. S19a, ESI†) while the XRD pattern reveals the preservation of the metallic Cu phase (Fig. S19b, ESI†).

To overcome the limit of  $CO_2$  solubility in aqueous solution and achieve higher current density, we evaluated the performance of catalysts in a home-made flow cell in 1 M  $KHCO_3$  solution. The working mechanism and EIS spectra of the flow cell are proposed and shown in Fig. S20 and S21 (ESI†), respectively. The chronoamperometry curves of Cu, Cu-1TA and Cu-3TA catalyst under different potentials are displayed in Fig. S22 (ESI†), where all current density surpasses  $-100 \text{ mA cm}^{-2}$  at applied potentials. The FE of  $C_2H_4$  is 43.54% at  $-0.85 \text{ V}$  for the Cu-1TA catalyst (Fig. 3e), which is higher than that for the Cu catalyst (the FE of  $C_2H_4$  is 27.07% at  $-0.85 \text{ V}$  in Fig. S23, ESI†). The sum of FE for  $C_{2+}$  is 65.57% for the Cu-1TA catalyst at  $-0.85 \text{ V}$ . Moreover, the current density of the Cu-1TA catalyst could attain  $-340 \text{ mA cm}^{-2}$  at  $-0.85 \text{ V}$  and partial current density for the  $C_{2+}$  products is  $-222.94 \text{ mA cm}^{-2}$ . Surprisingly, for the Cu-3TA catalyst (Fig. 3f), the FE of  $CH_4$  reaches up to 53.27% and the corresponding current density is about  $1000 \text{ mA cm}^{-2}$  at  $-1.05 \text{ V}$ , the partial current density for  $CH_4$  can reach up to  $532.70 \text{ mA cm}^{-2}$ . The result shows the highest partial current density of methane in the reported literature

(Table S2, ESI†). The higher FE of  $CH_4$  for the Cu-3TA catalyst in a flow cell might be attributed to the stronger buffering ability of 1 M  $KHCO_3$  than 0.1 M  $KHCO_3$ , which is conducive to  $CH_4$  formation.<sup>39</sup> Fig. S24 and S25 (ESI†) show the representative GC profiles of gaseous products and the corresponding concentration of Cu-1TA and Cu-3TA catalysts, clearly showing the transformation of selectivity between  $C_2H_4$  and  $CH_4$ . Fig. S26 (ESI†) shows the standard curves of  $CH_4$  and  $C_2H_4$  components for GC analysis. The product distribution in a flow cell again indicates that the selectivity of  $C_2H_4$  and  $CH_4$  could be tailored with increasing amounts of modified TA.

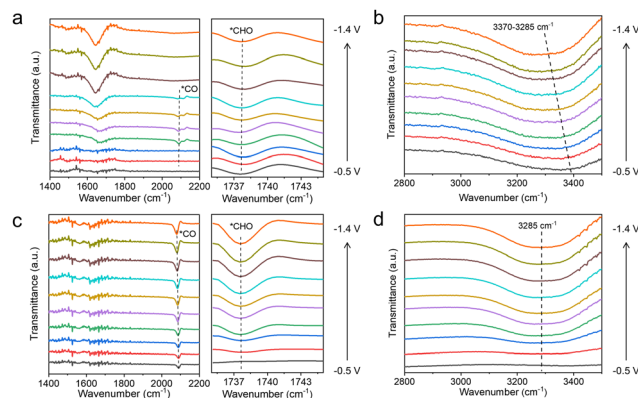


**Fig. 4** *In situ* attenuated total reflection surface-enhanced infrared absorption spectroscopy spectra of (a and b) Cu and (c and d) Cu-3TA catalysts in  $CO_2$ -saturated 0.1 M  $KHCO_3$  solution.

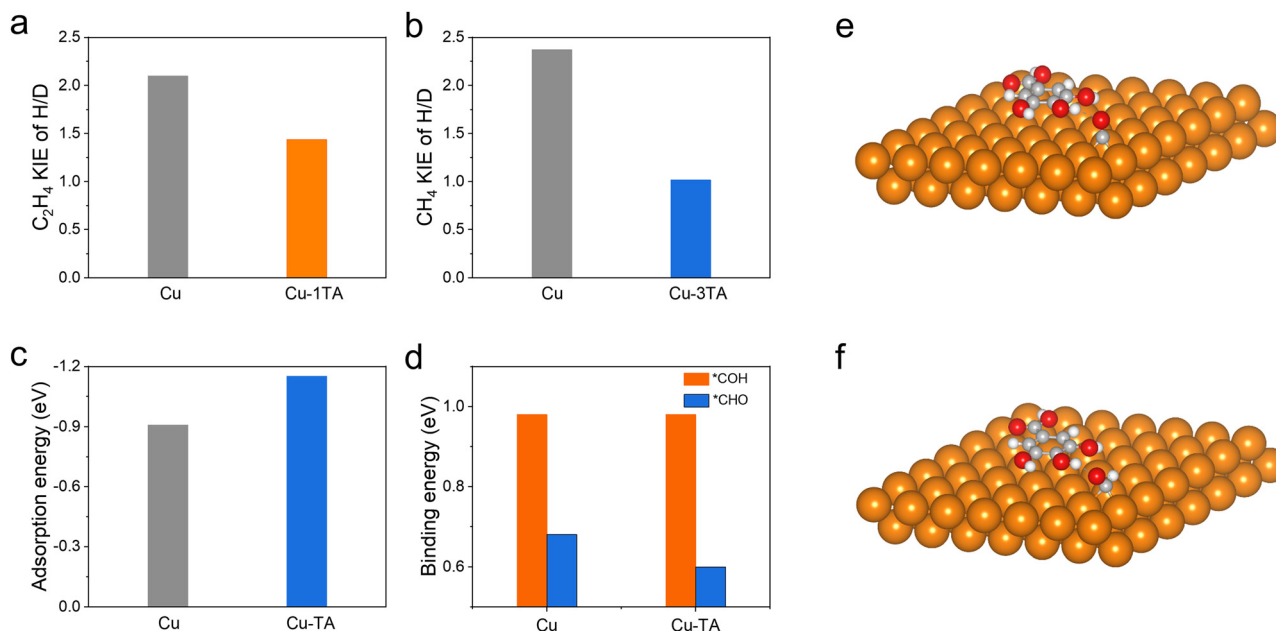


**Fig. 5** (a) Kinetic isotope effect (KIE) value of C<sub>2</sub>H<sub>4</sub> on Cu and Cu-1TA catalysts at  $-0.85$  V in a flow cell. (b) KIE value of CH<sub>4</sub> on Cu and Cu-3TA catalysts at  $-1.05$  V in a flow cell. (c) Calculated adsorption energy of \*CO on Cu and Cu-TA catalysts. (d) Binding energy from \*CO to \*COH or \*CHO intermediate on Cu and Cu-TA catalysts. (e and f) Optimized adsorption configuration of \*CO and \*CHO intermediates on the Cu-TA catalyst.

To clarify the effect of the TA molecule and the possible reaction mechanism of CO<sub>2</sub>RR in our work, we conducted *in situ* attenuated total reflection surface-enhanced infrared absorption spectroscopy (ATR-SEIRS) spectra to monitor intermediate behaviour on Cu, Cu-1TA and Cu-3TA catalysts. The photo and working mechanism of *in situ* ATR-SEIRS are shown in Fig. S27 (ESI<sup>†</sup>). From the spectra in Fig. 4a and c, we could see that there are two downward bands located at  $\sim 1738$  and  $\sim 2085$  cm<sup>-1</sup> in the Cu-3TA catalyst, respectively. The band at  $\sim 1738$  cm<sup>-1</sup> can be indexed as the stretching of \*CHO,<sup>40,41</sup> gradually increasing as the potentials become more negative. The band at  $\sim 2085$  cm<sup>-1</sup> is attributed to the linear-bond CO adsorption on the Cu surface.<sup>42,43</sup> The \*CO intermediate on the Cu-3TA catalyst possesses a stronger signal than the Cu catalyst, which demonstrates that TA modification can stabilize \*CO on the Cu surface, which is beneficial for further reaction to form the \*CHO intermediate. Thus, the Cu-3TA catalyst has a stronger signal about the \*CHO intermediate than the Cu catalyst. Fig. S28a (ESI<sup>†</sup>) shows the *in situ* ATR-SEIRS spectra, which reveal the presence of \*CO and \*CHO intermediates on the Cu-1TA catalyst.

The proton, participating in the formation of CO<sub>2</sub>RR products, comes from the dissociation of H<sub>2</sub>O<sup>44</sup> and it has been reported that hydrogen bonds could promote the proton transfer.<sup>45</sup> We then performed *in situ* ATR-SEIRS spectroscopy to investigate the change of hydrogen bonds after TA modification. For Cu-1TA and Cu-3TA catalysts, the stretching vibration of -OH in H<sub>2</sub>O shifts to a lower wavenumber at an earlier potential (Fig. 4b, d and Fig. S28b, ESI<sup>†</sup>). We consider that Cu-TA catalysts could enhance hydrogen bond interaction with H<sub>2</sub>O and promote proton transfer near the electrode surface.

Next, we carried out kinetic isotope effect (KIE) tests to explore how TA affects H<sub>2</sub>O dissociation on the Cu electrode.<sup>46,47</sup> We replace H<sub>2</sub>O with D<sub>2</sub>O as the solvent in 1 M KHCO<sub>3</sub> solution. The formation rate of C<sub>2</sub>H<sub>4</sub> and CH<sub>4</sub> drops more significantly for the Cu catalyst, whereas the formation rates of C<sub>2</sub>H<sub>4</sub> and CH<sub>4</sub> decline less for Cu-1TA and Cu-3TA catalysts (Fig. S29, ESI<sup>†</sup>), respectively. Fig. 5a and b show the calculated KIE values for C<sub>2</sub>H<sub>4</sub> and CH<sub>4</sub>. The KIE value of C<sub>2</sub>H<sub>4</sub> and CH<sub>4</sub> is 2.10 and 2.37 for the Cu catalyst, respectively, suggesting that the proton transfer is a rate-determining process, and the KIE value for Cu-1TA and Cu-3TA catalysts is determined to be 1.44 and 1.10, respectively. The smaller KIE value of Cu-TA catalyst than the Cu catalyst proves that the H<sub>2</sub>O dissociation process is not the rate-determining step, manifesting that TA-modified Cu could promote H<sub>2</sub>O to dissociate. The smallest KIE value for Cu-3TA reveals that the modification of more TA can activate more H<sub>2</sub>O and it could supply more protons for \*CO hydrogenation to form the \*CHO intermediate. Thus, the selectivity of CH<sub>4</sub> is enhanced with increasing amount of modified TA.

From the results of *in situ* ATR-SEIRS and KIE experiments, the TA-functionalized Cu electrode could not only stabilize the adsorbed \*CO intermediate, but also activate water dissociation to promote the PCET process. We propose that the \*CHO intermediate is prone to form on Cu-TA catalysts as compared to pristine Cu. In the case of less TA modification (*i.e.*, from Cu-0.5TA to Cu-2TA in Cu-*x*TA), \*CO would couple with \*CHO to form C<sub>2</sub>H<sub>4</sub> and the Cu-1TA catalyst exhibits the highest C<sub>2</sub>H<sub>4</sub> selectivity. However, more TA modification (*i.e.*, Cu-3TA and Cu-4TA) favours the formation of a hydrogen bond network, which facilitates proton transfer and water dissociation.<sup>27,28</sup> More protons would combine with \*CO to form more \*CHO

intermediate while more  $^*\text{CHO}$  species benefits  $\text{CH}_4$  generation. Therefore, the selectivity between  $\text{CH}_4$  and  $\text{C}_2\text{H}_4$  could be steered *via* altering the amount of modified TA. Then, we carried out DFT calculations to further unravel the origin of TA-modified Cu for tailoring the selectivity of hydrocarbons in  $\text{CO}_2\text{RR}$ . To simplify the TA molecule structure, we selected 3,4,5-trihydroxybenzoic acid as a molecular model because it is the monomer of TA hydrolysis. First, the possible adsorption configuration of TA on the (111) crystal plane of Cu NPs is optimized (Fig. S30, ESI<sup>†</sup>). Then, we calculated the adsorption free energies of the  $^*\text{CO}$  intermediate on Cu and Cu-TA NPs. The  $^*\text{CO}$  adsorption energy is found to be more negative on Cu-TA NPs (Fig. 5c and e), demonstrating that the  $^*\text{CO}$  intermediate could be stabilized on the Cu surface with TA modification. Next, we compared the binding energy of the  $^*\text{CO}$  to  $^*\text{CHO}$  or  $^*\text{COH}$  process. The optimized adsorption configurations are shown in Fig. 5f, Fig. S31 and S32 (ESI<sup>†</sup>), respectively. The binding energy from  $^*\text{CO}$  to  $^*\text{COH}$  is identical for Cu and Cu-TA NPs, while it decreases for Cu-TA NPs (Fig. 5d). The result indicates that the protonation process of  $^*\text{CO}$  to  $^*\text{CHO}$  is favoured for TA-modified Cu. From the above theoretical analysis, we confirm TA-modified Cu could stabilize  $^*\text{CO}$  and boost the  $^*\text{CHO}$  formation.

## Conclusions

In summary, we report the preparation of TA-modified Cu catalysts by simply mixing and ultrasound preparation for  $\text{CO}_2$  reduction. By controlling the amount of TA modification, we could achieve a considerable FE of  $\text{C}_2\text{H}_4$  (53.00%) for the Cu-1TA catalyst and FE of  $\text{CH}_4$  (53.27%) for the Cu-3TA catalyst, respectively. *In situ* ATR-SEIRS spectra show that TA modification could stabilize  $^*\text{CO}$  and  $^*\text{CHO}$  intermediates and enhance the hydrogen bond interaction with  $\text{H}_2\text{O}$  near the electrode surface. Kinetic tests further illustrate that TA modification can accelerate  $\text{H}_2\text{O}$  dissociation to supply indispensable protons to promote PCET. Furthermore, computational investigation indicates stabilization of the  $^*\text{CO}$  intermediate and lowering of the energy barrier for  $^*\text{CO}$  protonation to  $^*\text{CHO}$  after TA decoration. This study highlights an effective molecule modification strategy to tailor the  $\text{C}_2/\text{C}_1$  product selectivity *via* collectively stabilizing the  $^*\text{CO}$  intermediate and activating  $\text{H}_2\text{O}$  dissociation.

## Author contributions

K. X. and F. C. designed the study. K. X. prepared and characterized the materials, performed measurements, and drafted the manuscript. J. L. carried out DFT computations. F. C. supervised the research and co-wrote the paper. All authors contributed to data analysis and results discussion.

## Conflicts of interest

There are no conflicts to declare.

## Acknowledgements

This study was supported by NSFC (21835004, 21925503, 21871149, and 52001172), MOE (B12015), and the Fundamental Research Funds for the Central Universities. Computations were carried out on TianHe-1(A) at National Supercomputer Center in Tianjin.

## References

- 1 Y. Y. Birdja, E. Pérez-Gallent, M. C. Figueiredo, A. J. Göttele, F. Calle-Vallejo and M. T. M. Koper, Advances and challenges in understanding the electrocatalytic conversion of carbon dioxide to fuels, *Nat. Energy*, 2019, **4**, 732–745.
- 2 X. Tan, C. Yu, Y. Ren, S. Cui, W. Li and J. Qiu, Recent advances in innovative strategies for the  $\text{CO}_2$  electroreduction reaction, *Energy Environ. Sci.*, 2021, **14**, 765–780.
- 3 Y. Yan, L. W. Ke, Y. Ding, Y. Zhang, K. Rui, H. J. Lin and J. X. Zhu, Recent advances in Cu-based catalysts for electroreduction of carbon dioxide, *Mater. Chem. Front.*, 2021, **5**, 2668–2683.
- 4 Y. L. Shi, C. F. Wen, X. F. Wu, J. Y. Zhao, F. X. Mao, P. F. Liu and H. G. Yang, *In situ* reconstruction of vegetable sponge-like  $\text{Bi}_2\text{O}_3$  for efficient  $\text{CO}_2$  electroreduction to formate, *Mater. Chem. Front.*, 2022, **6**, 1091–1097.
- 5 H. Guo, D.-H. Si, H.-J. Zhu, Q.-X. Li, Y.-B. Huang and R. Cao, Ni single-atom sites supported on carbon aerogel for highly efficient electroreduction of carbon dioxide with industrial current densities, *eScience*, 2022, **2**, 295–303.
- 6 Z. Zhu, Z. Li, J. Wang, R. Li, H. Chen, Y. Li, J. S. Chen, R. Wu and Z. Wei, Improving  $\text{NiN}_x$  and pyridinic N active sites with space-confined pyrolysis for effective  $\text{CO}_2$  electroreduction, *eScience*, 2022, **2**, 445–452.
- 7 M. B. Ross, P. De Luna, Y. Li, C.-T. Dinh, D. Kim, P. Yang and E. H. Sargent, Designing materials for electrochemical carbon dioxide recycling, *Nat. Catal.*, 2019, **2**, 648–658.
- 8 R. Wang, T. Li, R. Gao, J. Qin, M. Li, Y. Guo and Y. Song, Carbonized Yolk-shell Metal-Organic Frameworks for Electrochemical Conversion of  $\text{CO}_2$  into Ethylene, *Chem. Res. Chin. Univ.*, 2022, DOI: [10.1007/s40242-022-2149-z](https://doi.org/10.1007/s40242-022-2149-z).
- 9 F. You, J. Wan, J. Qi, D. Mao, N. Yang, Q. Zhang, L. Gu and D. Wang, Lattice Distortion in Hollow Multi-Shelled Structures for Efficient Visible-Light  $\text{CO}_2$  Reduction with a  $\text{SnS}_2/\text{SnO}_2$  Junction, *Angew. Chem., Int. Ed.*, 2020, **59**, 721–724.
- 10 Z. Tao and H. Wang,  $\text{Pb}_3(\text{CO}_3)_2(\text{OH})_2$  is an Active Phase in Electrocatalytic  $\text{CO}_2$  Reduction to Formate, *Chem. Res. Chin. Univ.*, 2020, **36**, 1145–1146.
- 11 J. Yi, Q. Li, S. Chi, Y. Huang and R. Cao, Boron-doped Covalent Triazine Framework for Efficient  $\text{CO}_2$  Electroreduction, *Chem. Res. Chin. Univ.*, 2022, **38**, 141–146.
- 12 L. Wang, J. Wan, Y. Zhao, N. Yang and D. Wang, Hollow Multi-Shelled Structures of  $\text{CO}_3\text{O}_4$  Dodecahedron with Unique Crystal Orientation for Enhanced Photocatalytic  $\text{CO}_2$  Reduction, *J. Am. Chem. Soc.*, 2019, **141**, 2238–2241.
- 13 Y. Wei, F. You, D. Zhao, J. Wan, L. Gu and D. Wang, Heterogeneous Hollow Multi-Shelled Structures with Amorphous-

- Crystalline Outer-Shells for Sequential Photoreduction of CO<sub>2</sub>, *Angew. Chem., Int. Ed.*, 2022, **61**, e202212049.
- 14 W. Ma, X. He, W. Wang, S. Xie, Q. Zhang and Y. Wang, Electrocatalytic reduction of CO<sub>2</sub> and CO to multi-carbon compounds over Cu-based catalysts, *Chem. Soc. Rev.*, 2021, **50**, 12897–12914.
  - 15 B. Talukdar, S. Mendiratta, M. H. Huang and C.-H. Kuo, Recent Advances in Bimetallic Cu-Based Nanocrystals for Electrocatalytic CO<sub>2</sub> Conversion, *Chem. – Asian J.*, 2021, **16**, 2168–2184.
  - 16 W. Ma, S. Xie, X.-G. Zhang, F. Sun, J. Kang, Z. Jiang, Q. Zhang, D.-Y. Wu and Y. Wang, Promoting electrocatalytic CO<sub>2</sub> reduction to formate via sulfur-boosting water activation on indium surfaces, *Nat. Commun.*, 2019, **10**, 892.
  - 17 Y. Li, A. Xu, Y. Lum, X. Wang, S.-F. Hung, B. Chen, Z. Wang, Y. Xu, F. Li, J. Abed, J. E. Huang, A. S. Rasouli, J. Wicks, L. K. Sagar, T. Peng, A. H. Ip, D. Sinton, H. Jiang, C. Li and E. H. Sargent, Promoting CO<sub>2</sub> methanation via ligand-stabilized metal oxide clusters as hydrogen-donating motifs, *Nat. Commun.*, 2020, **11**, 6190.
  - 18 J. H. Montoya, A. A. Peterson and J. K. Nørskov, Insights into C=C Coupling in CO<sub>2</sub> Electroreduction on Copper Electrodes, *ChemCatChem*, 2013, **5**, 737–742.
  - 19 A. J. Garza, A. T. Bell and M. Head-Gordon, Mechanism of CO<sub>2</sub> Reduction at Copper Surfaces: Pathways to C<sub>2</sub> Products, *ACS Catal.*, 2018, **8**, 1490–1499.
  - 20 F. Li, A. Thevenon, A. Rosas-Hernández, Z. Wang, Y. Li, C. M. Gabardo, A. Ozden, C. T. Dinh, J. Li, Y. Wang, J. P. Edwards, Y. Xu, C. McCallum, L. Tao, Z.-Q. Liang, M. Luo, X. Wang, H. Li, C. P. O'Brien, C.-S. Tan, D.-H. Nam, R. Quintero-Bermudez, T.-T. Zhuang, Y. C. Li, Z. Han, R. D. Britt, D. Sinton, T. Agapie, J. C. Peters and E. H. Sargent, Molecular tuning of CO<sub>2</sub>-to-ethylene conversion, *Nature*, 2020, **577**, 509–513.
  - 21 D.-H. Nam, P. De Luna, A. Rosas-Hernández, A. Thevenon, F. Li, T. Agapie, J. C. Peters, O. Shekha, M. Eddaoudi and E. H. Sargent, Molecular enhancement of heterogeneous CO<sub>2</sub> reduction, *Nat. Mater.*, 2020, **19**, 266–276.
  - 22 M. S. Xie, B. Y. Xia, Y. Li, Y. Yan, Y. Yang, Q. Sun, S. H. Chan, A. Fisher and X. Wang, Amino acid modified copper electrodes for the enhanced selective electroreduction of carbon dioxide towards hydrocarbons, *Energy Environ. Sci.*, 2016, **9**, 1687–1695.
  - 23 S. Ahn, K. Klyukin, R. J. Wakeham, J. A. Rudd, A. R. Lewis, S. Alexander, F. Carla, V. Alexandrov and E. Andreoli, Poly-Amide Modified Copper Foam Electrodes for Enhanced Electrochemical Reduction of Carbon Dioxide, *ACS Catal.*, 2018, **8**, 4132–4142.
  - 24 Y. Ji, C. Yang, L. Qian, L. Zhang and G. Zheng, Promoting electrocatalytic carbon monoxide reduction to ethylene on copper-polypyrrole interface, *J. Colloid Interface Sci.*, 2021, **600**, 847–853.
  - 25 X. Wei, Z. Yin, K. Lyu, Z. Li, J. Gong, G. Wang, L. Xiao, J. Lu and L. Zhuang, Highly Selective Reduction of CO<sub>2</sub> to C<sub>2+</sub> Hydrocarbons at Copper/Polyaniline Interfaces, *ACS Catal.*, 2020, **10**, 4103–4111.
  - 26 X. Bai, L. Shi, Q. Li, C. Ling, Y. Ouyang, S. Wang and J. Wang, Synergistic Effect of Metal Doping and Tethered Ligand Promoted High-Selectivity Conversion of CO<sub>2</sub> to C<sub>2</sub> Oxygenates at Ultra-Low Potential, *Energy Environ. Mater.*, 2022, **5**, 892–898.
  - 27 Y.-R. Wang, M. Liu, G.-K. Gao, Y.-L. Yang, R.-X. Yang, H.-M. Ding, Y. Chen, S.-L. Li and Y.-Q. Lan, Implanting Numerous Hydrogen-Bonding Networks in a Cu-Porphyrin-Based Nanosheet to Boost CH<sub>4</sub> Selectivity in Neutral-Media CO<sub>2</sub> Electroreduction, *Angew. Chem., Int. Ed.*, 2021, **60**, 21952–21958.
  - 28 X. Li, B. Lv, X.-P. Zhang, X. Jin, K. Guo, D. Zhou, H. Bian, W. Zhang, U.-P. Apfel and R. Cao, Introducing Water-Network-Assisted Proton Transfer for Boosted Electrocatalytic Hydrogen Evolution with Cobalt Corrole, *Angew. Chem., Int. Ed.*, 2022, **61**, e202114310.
  - 29 C.-F. Li, J.-W. Zhao, L.-J. Xie, J.-Q. Wu, Q. Ren, Y. Wang and G.-R. Li, Surface-Adsorbed Carboxylate Ligands on Layered Double Hydroxides/Metal–Organic Frameworks Promote the Electrocatalytic Oxygen Evolution Reaction, *Angew. Chem., Int. Ed.*, 2021, **60**, 18129–18137.
  - 30 W. Li, F. Li, H. Yang, X. Wu, P. Zhang, Y. Shan and L. Sun, A bio-inspired coordination polymer as outstanding water oxidation catalyst via second coordination sphere engineering, *Nat. Commun.*, 2019, **10**, 5074.
  - 31 J.-D. Yi, R. Xie, Z.-L. Xie, G.-L. Chai, T.-F. Liu, R.-P. Chen, Y.-B. Huang and R. Cao, Highly Selective CO<sub>2</sub> Electroreduction to CH<sub>4</sub> by *In Situ* Generated Cu<sub>2</sub>O Single-Type Sites on a Conductive MOF: Stabilizing Key Intermediates with Hydrogen Bonding, *Angew. Chem., Int. Ed.*, 2020, **59**, 23641–23648.
  - 32 W. Yan, M. Shi, C. Dong, L. Liu and C. Gao, Applications of tannic acid in membrane technologies: A review, *Adv. Colloid Interface Sci.*, 2020, **284**, 102267.
  - 33 T. S. Sileika, D. G. Barrett, R. Zhang, K. H. A. Lau and P. B. Messersmith, Colorless Multifunctional Coatings Inspired by Polyphenols Found in Tea, Chocolate, and Wine, *Angew. Chem., Int. Ed.*, 2013, **52**, 10766–10770.
  - 34 B. Zhang, L. Qin, Y. Fang, Y. Chai, X. Xie, B. Lu, S. Liang and J. Zhou, Tuning Zn<sup>2+</sup> coordination tunnel by hierarchical gel electrolyte for dendrite-free zinc anode, *Sci. Bull.*, 2022, **67**, 955–962.
  - 35 H. Wang, X. Li, Y. Jiang, M. Li, Q. Xiao, T. Zhao, S. Yang, C. Qi, P. Qiu, J. Yang, Z. Jiang and W. Luo, A Universal Single-Atom Coating Strategy Based on Tannic Acid Chemistry for Multifunctional Heterogeneous Catalysis, *Angew. Chem., Int. Ed.*, 2022, **61**, e202200465.
  - 36 S. Thoka, M. Madasu, C.-F. Hsia, S.-Y. Liu and M. H. Huang, Aqueous-Phase Synthesis of Size-Tunable Copper Nanocubes for Efficient Aryl Alkyne Hydroboration, *Chem. – Asian J.*, 2017, **12**, 2318–2322.
  - 37 G. Zhang, Z.-J. Zhao, D. Cheng, H. Li, J. Yu, Q. Wang, H. Gao, J. Guo, H. Wang, G. A. Ozin, T. Wang and J. Gong, Efficient CO<sub>2</sub> electroreduction on facet-selective copper films with high conversion rate, *Nat. Commun.*, 2021, **12**, 5745.
  - 38 S. Zhang, P. Kang and T. J. Meyer, Nanostructured Tin Catalysts for Selective Electrochemical Reduction of Carbon Dioxide to Formate, *J. Am. Chem. Soc.*, 2014, **136**, 1734–1737.
  - 39 A. S. Varela, M. Kroschel, T. Reier and P. Strasser, Controlling the selectivity of CO<sub>2</sub> electroreduction on copper: The



- effect of the electrolyte concentration and the importance of the local pH, *Catal. Today*, 2016, **260**, 8–13.
- 40 L. Xiong, X. Zhang, H. Yuan, J. Wang, X. Yuan, Y. Lian, H. Jin, H. Sun, Z. Deng, D. Wang, J. Hu, H. Hu, J. Choi, J. Li, Y. Chen, J. Zhong, J. Guo, M. H. Rümmerli, L. Xu and Y. Peng, Breaking the Linear Scaling Relationship by Compositional and Structural Crafting of Ternary Cu–Au/Ag Nanoframes for Electrocatalytic Ethylene Production, *Angew. Chem., Int. Ed.*, 2021, **60**, 2508–2518.
  - 41 L. Xiong, X. Zhang, L. Chen, Z. Deng, S. Han, Y. Chen, J. Zhong, H. Sun, Y. Lian, B. Yang, X. Yuan, H. Yu, Y. Liu, X. Yang, J. Guo, M. H. Rummeli, Y. Jiao and Y. Peng, Geometric Modulation of Local CO Flux in Ag@Cu<sub>2</sub>O Nanoreactors for Steering the CO<sub>2</sub>RR Pathway toward High-Efficacy Methane Production, *Adv. Mater.*, 2021, **33**, 2101741.
  - 42 Z. Gu, H. Shen, Z. Chen, Y. Yang, C. Yang, Y. Ji, Y. Wang, C. Zhu, J. Liu, J. Li, T.-K. Sham, X. Xu and G. Zheng, Efficient Electrocatalytic CO<sub>2</sub> Reduction to C<sub>2+</sub> Alcohols at Defect-Site-Rich Cu Surface, *Joule*, 2021, **5**, 429–440.
  - 43 S. Zhu, B. Jiang, W.-B. Cai and M. Shao, Direct Observation on Reaction Intermediates and the Role of Bicarbonate Anions in CO<sub>2</sub> Electrochemical Reduction Reaction on Cu Surfaces, *J. Am. Chem. Soc.*, 2017, **139**, 15664–15667.
  - 44 M. C. O. Monteiro, F. Dattila, B. Hagedoorn, R. García-Muelas, N. López and M. T. M. Koper, Absence of CO<sub>2</sub> electroreduction on copper, gold and silver electrodes without metal cations in solution, *Nat. Catal.*, 2021, **4**, 654–662.
  - 45 M. E. Tuckerman, D. Marx and M. Parrinello, The nature and transport mechanism of hydrated hydroxide ions in aqueous solution, *Nature*, 2002, **417**, 925–929.
  - 46 W. Ma, S. Xie, T. Liu, Q. Fan, J. Ye, F. Sun, Z. Jiang, Q. Zhang, J. Cheng and Y. Wang, Electrocatalytic reduction of CO<sub>2</sub> to ethylene and ethanol through hydrogen-assisted C–C coupling over fluorine-modified copper, *Nat. Catal.*, 2020, **3**, 478–487.
  - 47 X. Yan, C. Chen, Y. Wu, S. Liu, Y. Chen, R. Feng, J. Zhang and B. Han, Efficient electroreduction of CO<sub>2</sub> to C<sub>2+</sub> products on CeO<sub>2</sub> modified CuO, *Chem. Sci.*, 2021, **12**, 6638–6645.